

Robin L. Tanamachi\*

Ming Xue

Youngsun Jung

Keith Brewster

*Center for Analysis and Prediction of Storms, University of Oklahoma, Norman, Oklahoma*

Michael I. Biggerstaff

*School of Meteorology, University of Oklahoma, Norman, Oklahoma*

## 1. INTRODUCTION

Recent efforts to include mobile and other non-standard ground-based radar data in ensemble analyses of severe convective storms have yielded promising results (e.g., Snook et al. 2011; Marquis et al. 2012; Tanamachi et al. 2012a). During VORTEX2 (Wurman et al. 2012), many severe convective storms, including tornadic supercells, were sampled comprehensively in both space and time by a fleet of mobile Doppler radars. This body of data provides a unique opportunity for data assimilation experiments incorporating multiple radar data sets of comparable spatial and temporal resolution.

For this study, we selected the case of the isolated, weakly tornadic 26 May 2010 Prospect Valley, Colorado supercell (hereafter “the Prospect Valley storm”; Fig. 1). Because of its relatively slow ( $5 \text{ m s}^{-1}$ ), steady, east-northeastward motion over relatively flat terrain, this storm was easily targeted by VORTEX2 teams. Although this storm did not produce any documented tornadoes during VORTEX2 operations (2100 on 26 May to 0041 UTC on 27 May), it did produce at least four tornadoes prior to operations, as well as several weak, tornado-like vortices (TLVs) around 2235 UTC (Tanamachi et al. 2012b, this volume).

We selected this case because radar spatial and temporal coverage of the Prospect Valley storm was exceptionally good. Near-continuous reflectivity, and Doppler velocity observations were made in the Prospect Valley storm by no fewer than 10 ground-based mobile Doppler radars. Some of these radars furnished polarimetric data, and many

collected over an hour of data. In addition, this storm was observed by WSR-88Ds at Denver, Colorado (KFTG), Pueblo, Colorado (KPX), and Cheyenne, Wyoming (KCYS), and a Terminal Doppler Weather Radar (TDWR) near Denver International Airport (TDEN). These overlapping data sets provide ample opportunity for independent verification, although we will only use a subset of these data here.

We used the ensemble square root Kalman filter (EnSRF) technique (Whitaker and Hamill 2002; Snyder and Zhang 2003) to assimilate mobile radar data onto a model grid with 250 m horizontal spacing, using the Advanced Regional Prediction System (Xue et al. 2003; Tong and Xue 2005) model to generate the short forecasts needed for analysis.

We assimilated data from two different types of mobile radars. The first were two C-band, Shared Mobile Atmospheric Research and Teaching Radars (SMART-Rs; Biggerstaff et al. 2005), which have half-power beamwidth of  $1.5^\circ$ . These two radars (hereafter denoted SR1 and SR2), were deployed along a 40 km long east-west baseline, collecting volume scans (containing multiple tilts from  $2.0^\circ$  upward) in the Prospect Valley storm every 3 min from 2227 UTC to 2327 UTC for dual-Doppler analysis (Fig. 1, Fig. 2). The second was the University of Massachusetts, mobile, W-band Doppler radar (UMW hereafter), which has half-power beamwidth of  $0.18^\circ$  and 30 m range gate spacing (Tsai et al. 2008). UMW had the highest spatial resolution in the VORTEX2 fleet and was used to collect near-surface sector scans in the potentially tornadic regions of target supercells (Fig. 2). Some examples of data collected by the latter radar are shown in Tanamachi et al. (2012b, this volume).

Near-surface flows are crucial to tornado formation and maintenance (e.g., Lewellen

---

\* Corresponding author's current affiliation: Robin L. Tanamachi; National Severe Storms Laboratory; 120 David L. Boren Blvd.; Norman, OK 73072; e-mail: [rtanamachi@ou.edu](mailto:rtanamachi@ou.edu)

and Lewellen 2007; Marquis et al. 2012). The authors suspect that information about this near-surface flow is crucial to making accurate forecasts of vortex formation. The primary questions driving this study are as follows: Does the assimilation of high-resolution, near-surface Doppler velocity data improve analyses of the hook region of a supercell spanning nearly 20 km in the vertical? Are the structures of the analyzed hook similar to those observed by high-resolution radars? How do the resulting analyses compare to independently collected radar observations?

This study is novel in that radar data collected within 150 m of the surface in a supercell hook echo are assimilated into a relatively high-resolution NWP model (250 m horizontal model grid spacing). Furthermore, in contrast to previous EnKF studies of severe convective storms initialized in a horizontally homogeneous environment (Marquis et al. 2008; Aksoy et al. 2009; Dowell and Wicker 2009; Yussouf and Stensrud 2010; Dawson et al. 2011; Dowell et al. 2011; Marquis et al. 2011; Tanamachi et al. 2012a), we use horizontally inhomogeneous initial conditions (background; e.g., Snook et al. 2011; Jung et al. 2012), in line with the recommendations of Stensrud and Gao (2010).

## 2. ARPSEnKF EXPERIMENT SETUP

An ensemble Kalman filter package has been developed and continually enhanced within the ARPS modeling framework (ARPSEnKF; Tong and Xue 2005; Xue et al. 2006). In order to capture the impact of the mesoscale environment on the limited domain over which we assimilated storm-scale radar data, we employed a triply-nested experiment domain. Each one-way nested grid inherited terrain, initial analysis background, and lateral boundary conditions from the next coarser one. The outermost grid, with 3 km horizontal grid spacing (domain size: 486 km x 366 km), was centered on the northeast quadrant of Colorado in order to cover the source region of low-level inflow air (eastern Colorado; Fig. 3). The two nested grids had horizontal grid spacing of 1 km (domain size: 162 km x 122 km) and 250 m (domain size: 80 km x 60 km), respectively. All three grids had the same stretched vertical terrain-following model levels; the near-surface vertical grid spacing was 50 m (Table 1).

A flow diagram for this setup is shown in Fig. 4. Our background state was interpolated

from the operational North American Mesoscale (NAM) model, which provides observation-derived analyses of the atmospheric state every 6 h, and forecasts every 3 h after each analysis, providing lateral boundary conditions for our coarsest grid every 3 h. Our experiment commenced at 1800 UTC on 26 May when a 3 km ensemble was launched from a perturbed 1800 UTC operational NAM analysis. The experiment continued through 0000 UTC on 27 May, encompassing the time of the VORTEX2 operations and data collection. KCYS and KPUX (KFTG) reflectivity ( $Z$ ) and Doppler velocity ( $V_r$ ) observations were then assimilated on the 3 km (1 km) grid in 5-min cycles starting at 1930 UTC (2100 UTC). The assumed observation errors for WSR-88D  $Z$  and  $V_r$  were 5 dBZ and 2 m s<sup>-1</sup>, respectively.

On the 250 m grid, SR1  $Z$  and  $V_r$  observations were assimilated in 3-min cycles starting at 2227 UTC. The assumed observation errors for  $Z$  and  $V_r$  for the mobile radar data were increased to 9 dBZ and 3 m s<sup>-1</sup>, respectively, values that have been shown to improve ensemble innovation and spread statistics when a relatively simple microphysical parameterization scheme, such as the Lin et al. (1983) scheme, is used on a storm-scale grid (N. Snook 2012, personal communication). Additive noise (Caya et al. 2005) and multiplicative inflation (Anderson 2001) were also used to help maintain ensemble spread. We focus exclusively on experiments on the 250 m grid for the remainder of this paper.

We ran four different data assimilation experiments on the 250 m grid. The first (control) experiment **SR1**, was conducted exactly as described above. In the other three, additional  $V_r$  observations from other radars were assimilated. We label these experiments according to radar observations assimilated: **SR1SR2**, **SR1UMW**, and **SR1SR2UMW**. We note here a gap in SR2 volumetric coverage early in the assimilation cycles (Fig. 5). Only single-elevation scans were collected in the three SR2 volumes starting at 2233, 2236, and 2239 UTC; these observations were not assimilated but were used for verification.

## 3. RESULTS

The overall location, size, and structure of the Prospect Valley supercell was accurately analyzed in all four experiments, with surrounding convection suppressed by

assimilation of low-reflectivity (no precipitation) data (Fig. 6). Detailed hook echo structure including RFDs (not shown) and vorticity maxima (Fig. 7), were evident in the ensemble mean.

As expected, assimilation of different subsets of radar data substantially altered vorticity in the hook echo. The near-surface TLV was best reproduced (in terms of location, structure, and vorticity) in experiment SR1UMW. This result was somewhat surprising; we had expected that the SR1SR2UMW experiment, assimilating the greatest number of velocity observations, would generate the strongest representation of the TLV. We speculate that because the TLV was not well resolved in either the SR1 or SR2 data, and because many more SR1 and SR2 observations were assimilated than UMW observations, the TLV was not well-represented in the analysis state. The analyses at all altitudes were dominated by the volumetric SR1 and SR2 observations (which had a vertical localization radius of 1.5 km; Table 1). UMW observations, which were collected at only one elevation angle (Fig. 2), were too weakly weighted in the calculation of the analysis state. One possible remedy would be to thin (or super-ob) the SR1 and SR2 observations, thereby increasing the influence of the UMW observations.

#### 4. OBSERVATION-SPACE DIAGNOSTICS

We use the observation-space diagnostic quantity consistency ratio (CR) defined by Dowell and Wicker (2009) to quantitatively evaluate the ensemble. CR values close to 1.0 are desirable because they indicate that the ensemble total spread is comparable to the assumed observation error for  $V_r$  ( $3 \text{ m s}^{-1}$ ). We calculated CR within the 15 dBZ isosurface using  $V_r$  observations from the SR1, SR2, KFTG, and UMW radars (Fig. 8). The reader should bear in mind that there are far fewer UMW observations available for verification relative to the other radars owing to its single-elevation scanning strategy (Fig. 2), so the CR for all experiments should be expected to be noisy.

The ensembles generally showed good dispersion in all four experiments, trending from underdispersed ( $\text{CR} < 1.0$ ) towards unity with time. That the CR statistics are consistently close to unity when verified against KFTG data, which were independently collected and not assimilated on the 250 m

grid, lends confidence to the ensemble forecasts.

The domain-wide root mean squared innovations (RMSI) and spread calculated against KFTG observations (Fig. 9) also exhibited some intriguing trends. First, the additional assimilation of SR2 data decreased both RMSI and spread for both analyses and forecasts at times when SR2 collected volumetric data (Fig. 5). This result is consistent with the results from Potvin and Wicker (2012), who found (in OSSE experiments) that EnKF retrievals of supercell winds were generally better when volumetric observations from two radars, rather than one radar, were assimilated.

Second, assimilation of UMW observations had very little effect on the RMSI, but increased the spread by about  $1 \text{ m s}^{-1}$  in most cycles relative to those experiments in which UMW data were withheld. The consistency ratio also trended toward unity faster in experiments SR1UMW and SR1SR2UMW (Fig. 8c). Experiment SR1UMW, in particular, showed nearly optimal dispersion (i.e., spread close to  $3 \text{ m s}^{-1}$ ). The reasons for this domain-wide increase in spread are not entirely clear. UMW  $V_r$  data contained information about small-scale, near-surface, near-updraft wind features such as the TLV. We speculate that the effects of these features were amplified by the model with each forecast cycle, thereby increasing the ensemble spread. This result suggests a potentially novel means of increasing ensemble spread: assimilating near-surface radar observations beneath convective storms when they are available.

#### 5. TRAJECTORY ANALYSES

In each ensemble member prior state at 2236 UTC, we initialized three sets (from 50 m, 150 m, and 1 km AGL) of 3 min *backward* trajectories from a 300-m diameter ring around the vorticity maximum corresponding to the TLV. The trajectories, calculated at 5-sec intervals, exhibited great variability in shape and origin (not shown).

The origin of air entering the vortex depended on the height at which the trajectories were initialized. Air entering the vortex at 50 m AGL originated near the surface, and converged on the vortex from all directions. Roughly half of the trajectories originated above and the level where the trajectories were initialized in the SR1

experiment (Fig. 10). Assimilation of additional radar data caused the fraction of ascending trajectories to increase slightly. Similar results were obtained for the trajectories initialized at 150 m AGL.

In contrast, air entering the vorticity maximum at 1 km AGL originated from two principal sources: (1) descending into the vortex from the west or northwest in the RFD, or (2) ascending into the vortex from the inflow sector. The descending trajectories dominated in all but one of the experiments (SR1SR2).

Our results contrast with those of Dahl et al. (2012), who found in idealized simulations that trajectories entering a simulated vortex near the surface originated almost exclusively from the RFD, whereas those entering the low-level mesocyclone from the inflow sector were drawn up over the gust front and their associated vorticity ultimately augmented the low-level mesocyclone. Our analyses were of a real case and included the assimilation of volumetric radar data. That the relative proportions of ascending and descending trajectories were so strongly dependent upon the radar data sets being assimilated is a finding which merits further investigation.

We calculated circulation around these trajectory rings as a function of time, then calculated the mean over the ensemble. Circulation around these trajectory rings was, on average, largest in the SR1UMW experiment (Fig. 11). We speculate that the additional assimilation of UMW data better defined the TLV in the ensemble of model states. However, this result does not hold for experiment SR1SR2UMW, whose trajectories had the smallest circulations. We speculate that the additional assimilation of the SR2 data resulted in poorer analysis of the TLV.

## 6. CONCLUSIONS

Comprehensive multi-Doppler radar coverage of the 26 May 2010 Prospect Valley, Colorado storm allowed for detailed EnKF analyses of the storm to be generated and verified against independently collected, volumetric radar data.

- EnKF analyses of the Prospect Valley storm generated from dual SR volumes (SR1SR2 and SR1SR2UMW) more accurately analyzed the overall hook echo structure (e.g., vorticity maxima; Fig. 7) than those in which SR2 data were withheld (SR1 and SR1UMW, respectively).

- TLV 5 was best reproduced in the SR1UMW experiment (Fig 6c), where one volume scan and one low-level single-elevation scan were assimilated each cycle. Assimilating an additional volume scan (i.e., SR1SR2UMW) was actually detrimental to analysis of these structures (Fig. 7).
- Additional assimilation of single, low-elevation scans from UMW (SR1UMW and SR1SR2UMW) improved ensemble spread (and consistency ratio) over those experiments in which only volume scans from SRs were assimilated (SR1 and SR1SR2, respectively), while having minimal impact on the RMS innovations (Fig. 9). This suggests a potentially novel method of ensemble spread improvement.
- Air entering TLV 5 at different levels came from distinct sources:
  - Backwards trajectories initialized near TLV 5 at  $\leq 150$  m AGL tended to originate near the surface and ascend slightly as they approached the vortex.
  - In three of the four experiments, approximately two-third of backwards trajectories initialized from near the hook tip vortex at 1 km AGL originated from descending flow in the RFD, while the remaining one-third ascended into the vortex from the inflow sector (Fig. 10). The exception was experiment SR1SR2, in which the opposite occurred. The reason for this difference is unclear at this time.
- Mean circulation around the backwards trajectory rings was strongest in experiment SR1UMW, possibly reflecting superior analysis of TLV5 in the previous assimilation cycle (Fig. 11).

## 7. ACKNOWLEDGMENTS

This research was supported principally by National Science Foundation (NSF) grant AGS-0802888. Drs. Yunheng Wang and Nathan Snook instructed the first author in the use of ARPSEnKF. Mr. Scott Hill provided computing support. Simulations were conducted using the supercomputing resources and guidance of the Oklahoma Supercomputing Center for Education and Research (OSCER), under the directorship of Dr. Henry Neeman. Radar data collection during VORTEX2 was supported by NSF grants ATM-0637148, AGS-0934307, and AGS-0802717. Gordon Carrie shared SMART-

R data, which were edited by Efren Afante. Dr. Howard Bluestein provided access to the UMW data. The National Climatic Data Center furnished WSR-88D data. Additional data were furnished by NCAR/EOL, under sponsorship of the NSF.

## 8. REFERENCES

- Aksoy, A., D. C. Dowell, and C. Snyder, 2009: A multicas e comparative assessment of the ensemble Kalman filter for assimilation of radar observations. Part I: Storm-scale analyses. *Mon. Wea. Rev.*, **137**, 1805-1824.
- Anderson, J. L., 2001: An ensemble adjustment Kalman filter for data assimilation. *Mon. Wea. Rev.*, **129**, 2884-2903.
- Biggerstaff, M. I., L. J. Wicker, J. Guynes, C. Ziegler, J. M. Straka, E. N. Rasmussen, A. Doggett, L. D. Carey, J. L. Schroeder, and C. Weiss, 2005: The Shared Mobile Atmospheric Research and Teaching Radar: A collaboration to enhance research and teaching. *Bull. Amer. Meteor. Soc.*, **86**, 1263-1274.
- Caya, A., J. Sun, and C. Snyder, 2005: A comparison between the 4DVAR and the ensemble Kalman filter techniques for radar data assimilation. *Mon. Wea. Rev.*, **133**, 3081-3094.
- Dahl, J. M. L., M. D. Parker, and L. J. Wicker, 2012: Uncertainties in trajectory calculations within near-surface mesocyclones of simulated supercells. *Mon. Wea. Rev.*, accepted.
- Dawson, D. T., L. J. Wicker, E. R. Mansell, and R. L. Tanamachi, 2011: Impact of the environmental low-level wind profile on ensemble forecasts of the 4 May 2007 Greensburg, Kansas tornadic storm and associated mesocyclones. *Mon. Wea. Rev.*, accepted.
- Dowell, D. C., and L. J. Wicker, 2009: Additive noise for storm-scale ensemble data assimilation. *J. Atmos. Oceanic Technol.*, **26**, 911-927.
- Dowell, D. C., L. J. Wicker, and C. Snyder, 2011: Ensemble Kalman filter assimilation of radar observations of the 8 May 2003 Oklahoma City supercell: Influences of reflectivity observations on storm-scale analyses. *Mon. Wea. Rev.*, **139**, 272-294.
- Jung, Y., M. Xue, and M. Tong, 2012: Ensemble Kalman filter analyses of the 29-30 May 2004 Oklahoma tornadic thunderstorm using one- and two-moment bulk microphysics schemes, with verification against polarimetric radar data. *Mon. Wea. Rev.*, **140**, 1457-1475.
- Lewellen, D. C., and W. S. Lewellen, 2007: Near-surface vortex intensification through corner flow collapse. *J. Atmos. Sci.*, **64**, 2195-2209.
- Lin, Y.-L., R. D. Farley, and H. D. Orville, 1983: Bulk parameterization of the snow field in a cloud model. *J. Appl. Meteor.*, **22**, 1065-1092.
- Marquis, J., Y. Richardson, J. Wurman, P. Markowski, and D. C. Dowell, 2008: Mobile radar observations of tornadic supercells with multiple rear-flank gust fronts. *24th Conf. on Severe Local Storms*, Savannah, Georgia, American Meteorological Society, 19.13.
- Marquis, J., Y. Richardson, P. M. Markowski, D. C. Dowell, and J. Wurman, 2011: Tornado maintenance investigated with high-resolution dual-Doppler and EnKF analysis. *Mon. Wea. Rev.*, in press.
- Marquis, J., Y. Richardson, P. Markowski, D. Dowell, and J. Wurman, 2012: Tornado maintenance investigated with high-resolution dual-Doppler and EnKF analysis. *Mon. Wea. Rev.*, **140**, 3-27.
- Potvin, C. K., and L. J. Wicker, 2012: Comparison between dual-Doppler and EnKF storm-scale wind analyses: Observing system simulation experiments with a supercell thunderstorm. *Mon. Wea. Rev.*, **140**, 3972-3991.
- Snook, N. A., M. Xue, and Y. Jung, 2011: Analysis of a tornadic mesoscale convective vortex assimilating CASA X-band and WSR-88D radar data using an ensemble Kalman filter. *Mon. Wea. Rev.*, **139**, 3446-3468.
- Snyder, C., and F. Zhang, 2003: Assimilation of simulated Doppler radar observations with an ensemble Kalman filter. *Mon. Wea. Rev.*, **131**, 1663-1677.
- Stensrud, D. J., and J. Gao, 2010: Importance of horizontally inhomogeneous environmental initial conditions to ensemble storm-scale radar data assimilation and very short-range forecasts. *Mon. Wea. Rev.*, **138**, 1250-1272.
- Tanamachi, R. L., L. J. Wicker, D. C. Dowell, H. B. Bluestein, and M. Xue, 2012a: EnKF assimilation of high-resolution, mobile Doppler radar data of the 4 May 2007 Greensburg, Kansas supercell into a numerical cloud model. *Mon. Wea. Rev.*, in press.
- Tanamachi, R. L., H. B. Bluestein, K. A. Orzel, S. J. Frasier, and M. Xue, 2012b: GBVTD-retrieved near-surface axisymmetric vortex structure in a tornado and tornado-like vortices

- observed by a W-band radar during VORTEX2. *26th Conf. on Severe Local Storms*, Nashville, Tennessee, American Meteorological Society, 14.11.
- Tong, M., and M. Xue, 2005: Ensemble Kalman filter assimilation of Doppler radar data with a compressible nonhydrostatic model: OSS experiments. *Mon. Wea. Rev.*, **133**, 1789-1807.
- Tsai, P., S. Frasier, R. L. Tanamachi, and H. B. Bluestein, 2008: The UMass mobile W-Band Doppler radar: System overview and sample observations. *24th Conf. on Severe Local Storms*, Savannah, Georgia, American Meteorological Society, P13.15.
- Whitaker, J. S., and T. M. Hamill, 2002: Ensemble data assimilation without perturbed observations. *Mon. Wea. Rev.*, **130**, 1913-1924.
- Wurman, J., D. Dowell, Y. Richardson, P. Markowski, E. Rasmussen, D. Burgess, L. Wicker, and H. B. Bluestein, 2012: The Second Verification of the Origins of Rotation in Tornadoes Experiment: VORTEX2. *Bull. Amer. Meteor. Soc.*, **93**, 1147-1170.
- Xue, M., M. Tong, and K. K. Droegemeier, 2006: An OSSE framework based on the ensemble square root Kalman filter for evaluating the impact of data from radar networks on thunderstorm analysis and forecasting. *J. Atmos. Oceanic Technol.*, **23**, 46-66.
- Xue, M., D. Wang, J. Gao, K. Brewster, and K. K. Droegemeier, 2003: The Advanced Regional Prediction System (ARPS), storm-scale numerical weather prediction and data assimilation. *Meteor. Atmos. Phys.*, **82**, 139-170.
- Yussouf, N., and D. J. Stensrud, 2010: Impact of phased-array radar observations over a short assimilation period: Observing system simulation experiments using an ensemble Kalman filter. *Mon. Wea. Rev.*, **138**, 517-538.

**Table 1. Experiment parameters used on the nested horizontal grids.**

<b>Horizontal grid spacing</b>	<b>3 km</b>	<b>1 km</b>	<b>250 m</b>
Radar data assimilated	KCYS, KPUX	KFTG	SR1, SR2, UMW
Observation types assimilated	$Z, V_r$	$Z, V_r$	$Z, V_r$
Assimilation period	1930 – 0000 UTC	2100 – 0000 UTC	2227 – 2327 UTC
Assimilation cycle frequency	5 min	5 min	3 min
Simulation domain	486 km × 366 km × 25 km	162 km × 122 km × 25 km	80 km × 60 km × 25 km
Domain grid points	163 × 123 × 51	163 × 123 × 51	323 × 243 × 51
Center of domain	39.5 °N, 103.5 °W	40.07 °N, 104.30 °W	40.20 °N, 104.29 °W
LBC source (frequency)	NAM (3 hr)	3 km (5 min)	1 km (5 min)
Spread maintenance method (standard deviation)	Multiplicative inflation factor = 1.2 <b>1800 UTC:</b> Domain-wide Gaussian perturbations to $u, v$ ( $0.5 \text{ m s}^{-1}$ ), $\theta$ (0.25 K) <b>1920 UTC:</b> Domain-wide Gaussian perturbations to $u, v$ ( $0.5 \text{ m s}^{-1}$ ), $q_v$ (0.0001 $\text{kg kg}^{-1}$ ), and $\theta$ (0.25 K) where $Z > 0 \text{ dBZ}$	Multiplicative inflation factor = 1.2	Multiplicative inflation factor = 1.2, Domain-wide random additive noise applied to $u, v$ ( $2.0 \text{ m s}^{-1}$ ), $\theta$ (0.5 K)
Model time step	5 sec	3 sec	0.5 sec
Assumed observation error variance for $Z$ ( $\sigma_z^2$ ) and $V_r$ ( $\sigma_{vr}^2$ )	$(5.0 \text{ dBZ})^2, (2.0 \text{ m s}^{-1})^2$	$(5.0 \text{ dBZ})^2, (2.0 \text{ m s}^{-1})^2$	$(9.0 \text{ dBZ})^2, (3.0 \text{ m s}^{-1})^2$



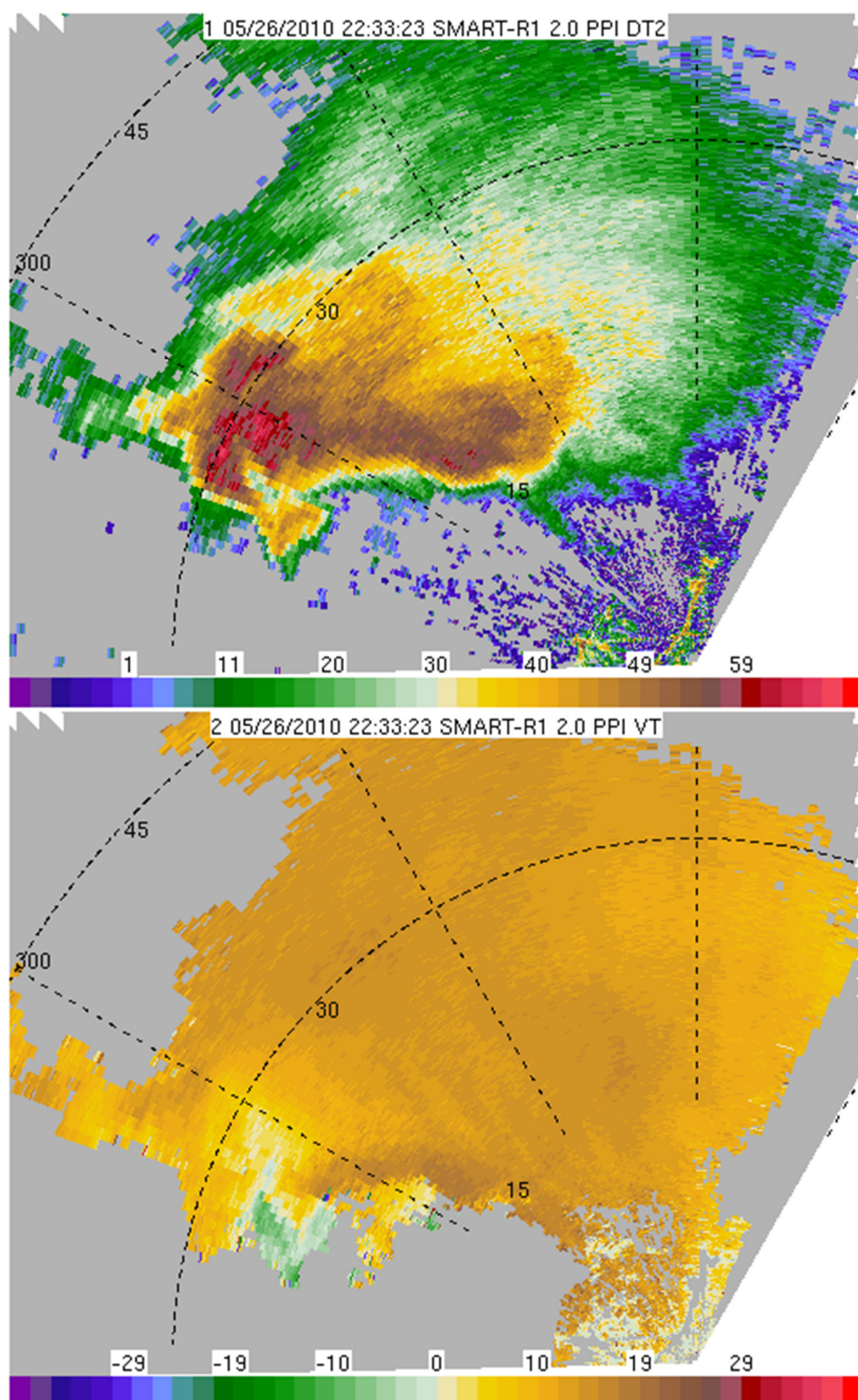
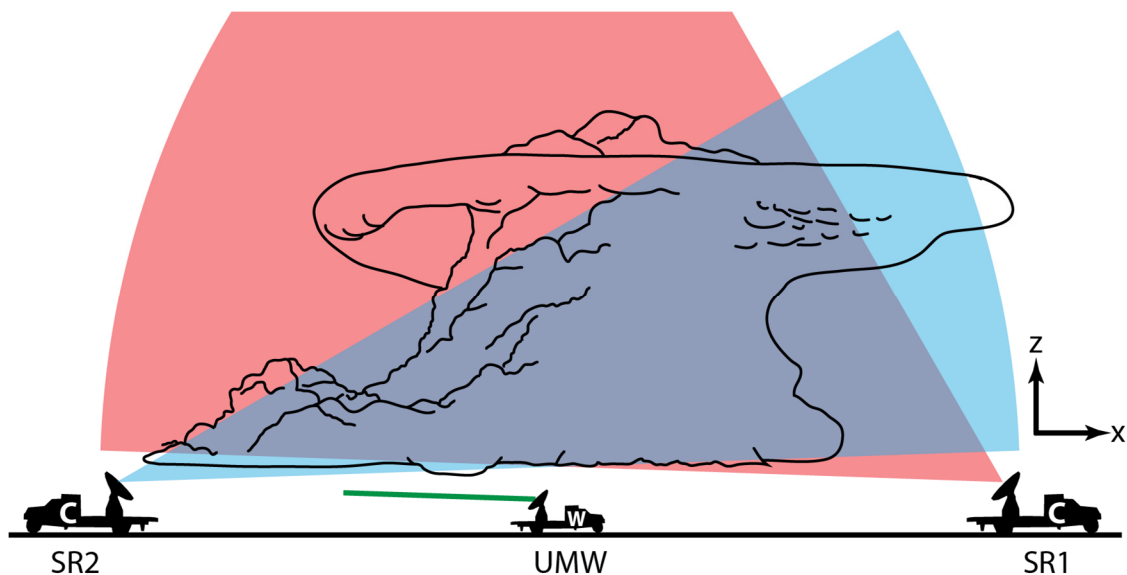
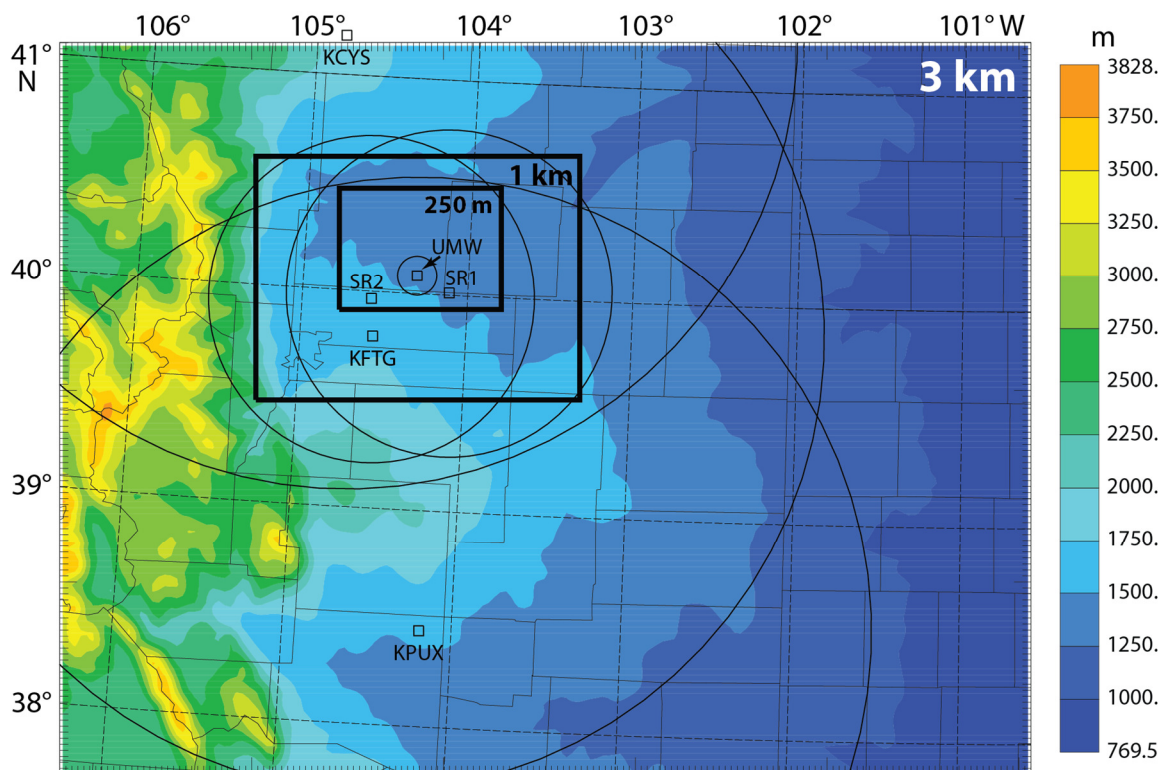


Fig. 1. (top) Reflectivity (in dBZ) and (bottom) Doppler velocity (in  $\text{m s}^{-1}$ ) observations from SR1 (elevation angle  $2.0^\circ$ ) of the Prospect Valley storm at 2233 UTC on 26 May 2010, when TLVs were observed. Some clutter can be seen near the radar (located at the origin). Range rings (azimuth spokes) are 15 km ( $30^\circ$ ) apart.





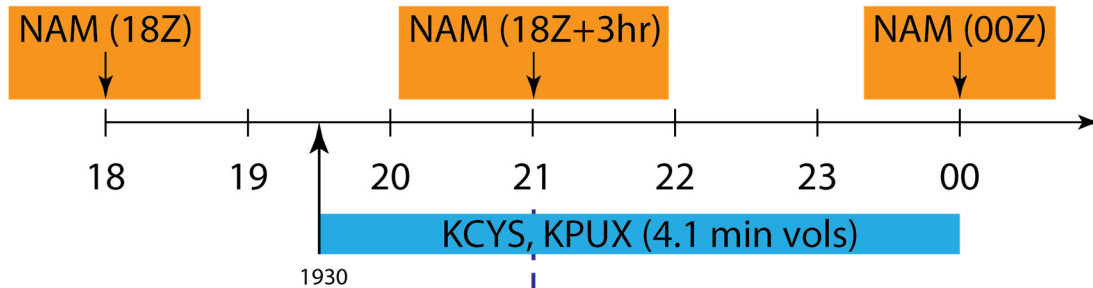
**Fig. 2. Schematic illustration of radar coverage for this case (not to scale). SR1 and SR2 collected volume scans (red and blue, respectively) of the Prospect Valley storm every 3 min, while UMW collected short-range, single-elevation scans (green) beneath the hook echo and wall cloud of the Prospect Valley storm.**



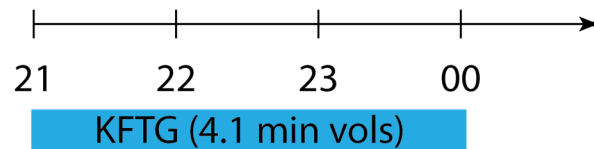
**Fig. 3. Nested experiment domain in northeast Colorado. Colored shadings represent terrain height. Maximum range rings are shown for each radar. Note that although a full 360-degree range ring is shown for UMW, it only collected sectors at a single elevation angle.**

# 26 May 2010 Experiment Setup

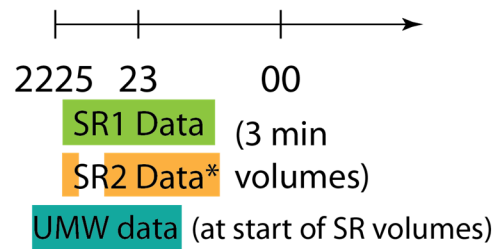
3 km: Assimilate Z and Vr data from KCYS and KPUX



1 km: Assimilate Z and Vr data from KFTG



250 m: Assimilate Z and Vr data from SR1,  
Vr data from SR2 and UMW



\* SR2 data contain a 10-minute gap

Fig. 4. Flow diagram for our experiment.

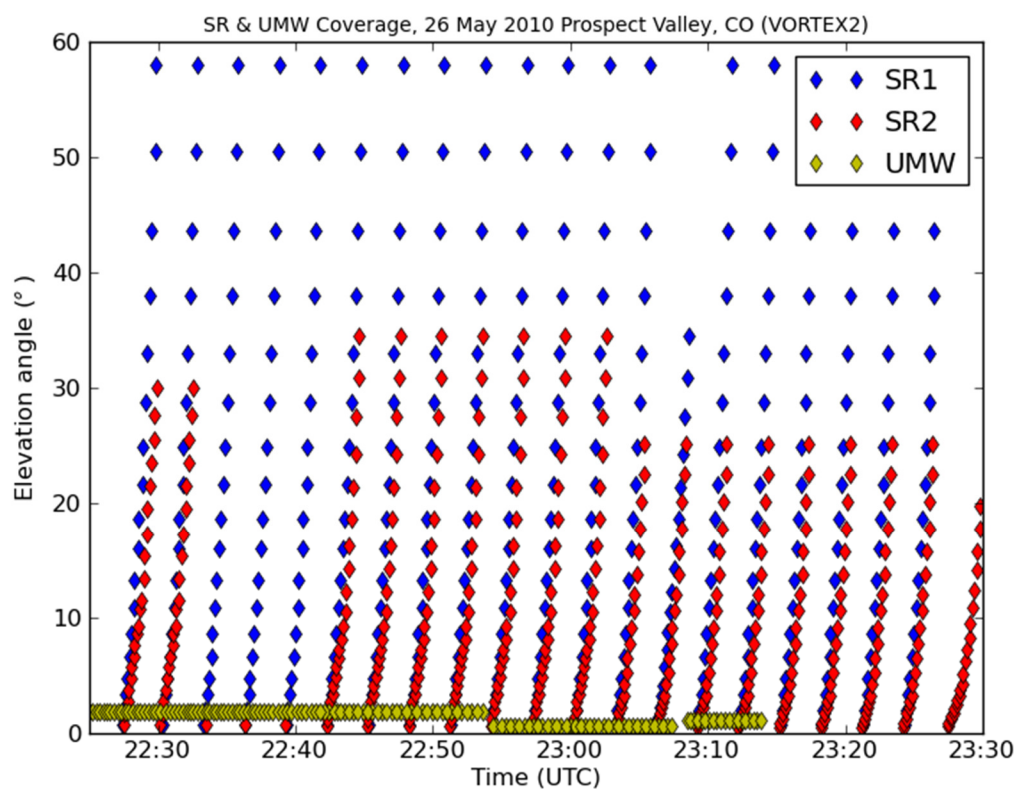


**Fig. 5. Volume coverage patterns for SR1 (blue), SR2 (red), and UMW (yellow) as a function of time. Note the gap in SR2 volumetric coverage from 2233-2242 UTC. Only the UMW scans closest to the start time of each SR volume were assimilated.**

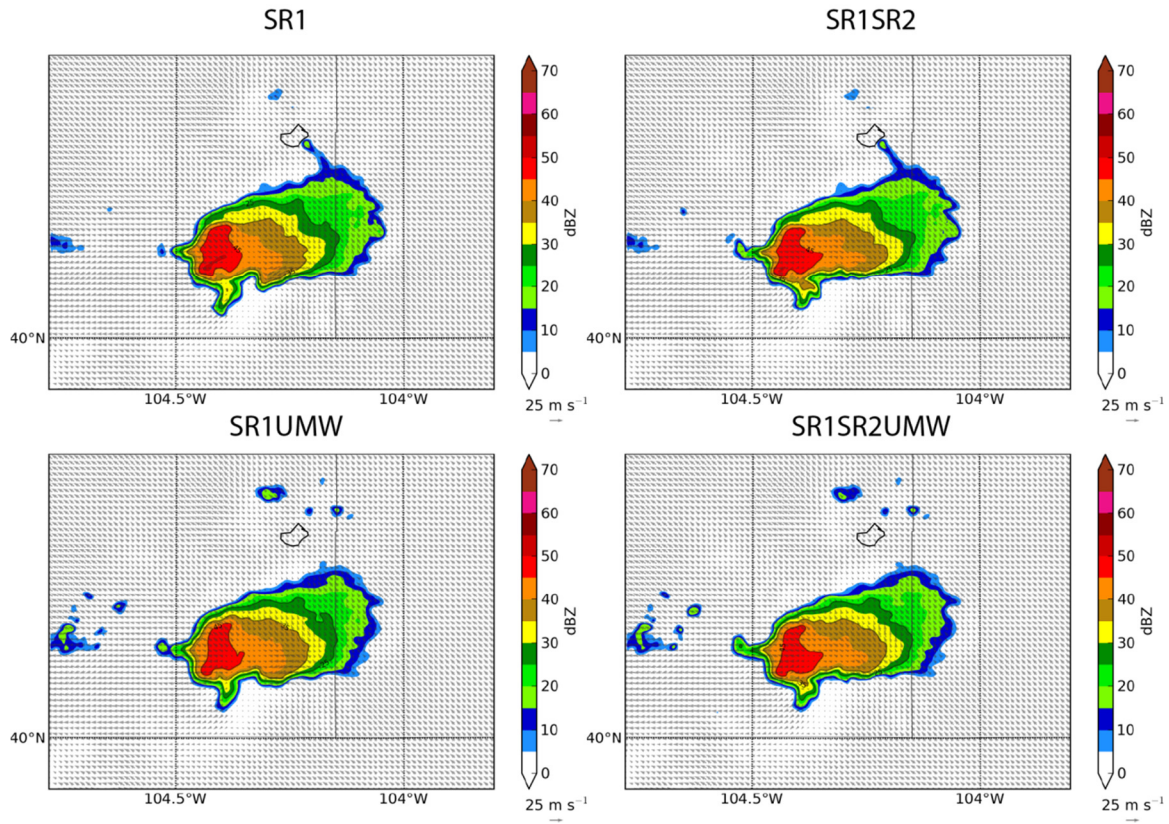


**Fig. 6. Prior ensemble mean reflectivity (in dBZ) and storm-relative wind vectors (in  $\text{m s}^{-1}$ , plotted every 4 km) at 50 m AGL on the 250 m domain at 2236 UTC.**



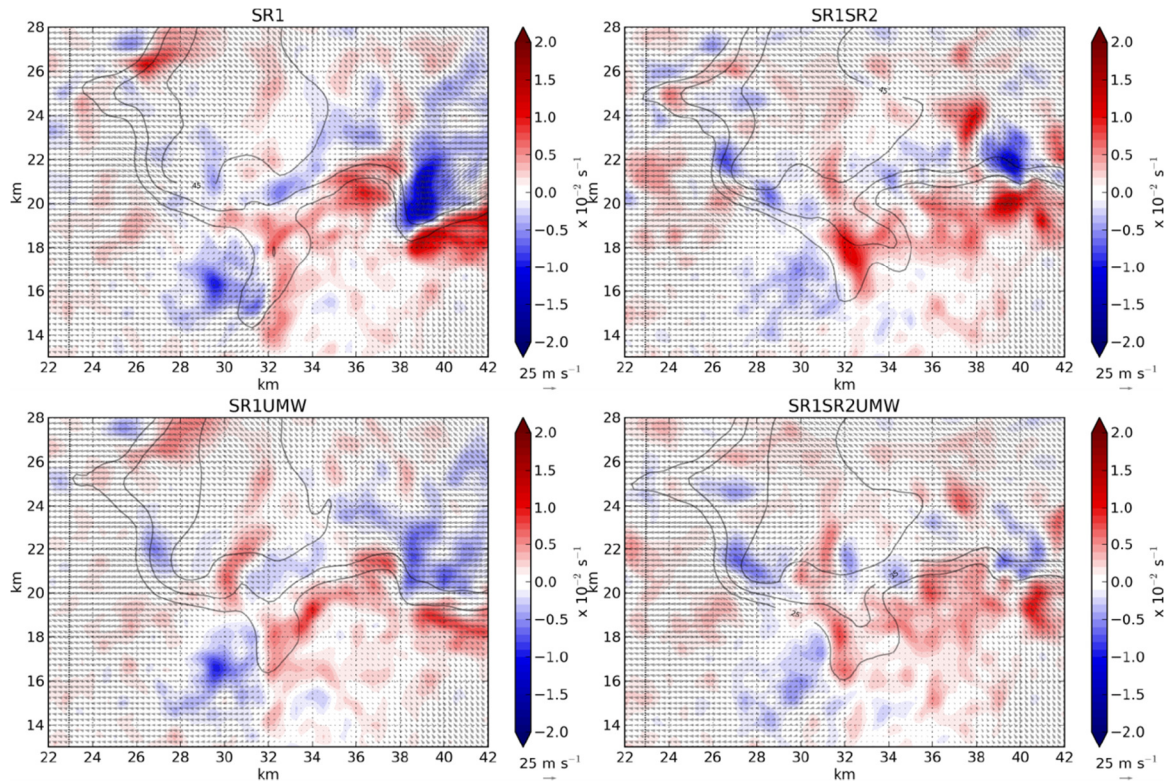


**Fig. 7. Prior ensemble mean vorticity (in  $10^{-2} \times \text{s}^{-1}$ ) and storm-relative wind vectors (in  $\text{m s}^{-1}$ , plotted at every grid point) at 150 m AGL at 2236 UTC. Reflectivity contours (intervals of 15 dBZ) are overlaid. The view is enlarged relative to that in Fig. 6. We expect to find a vorticity maximum corresponding to the TLV near  $x = 34.5 \text{ km}$ ,  $y = 19.0 \text{ km}$ .**

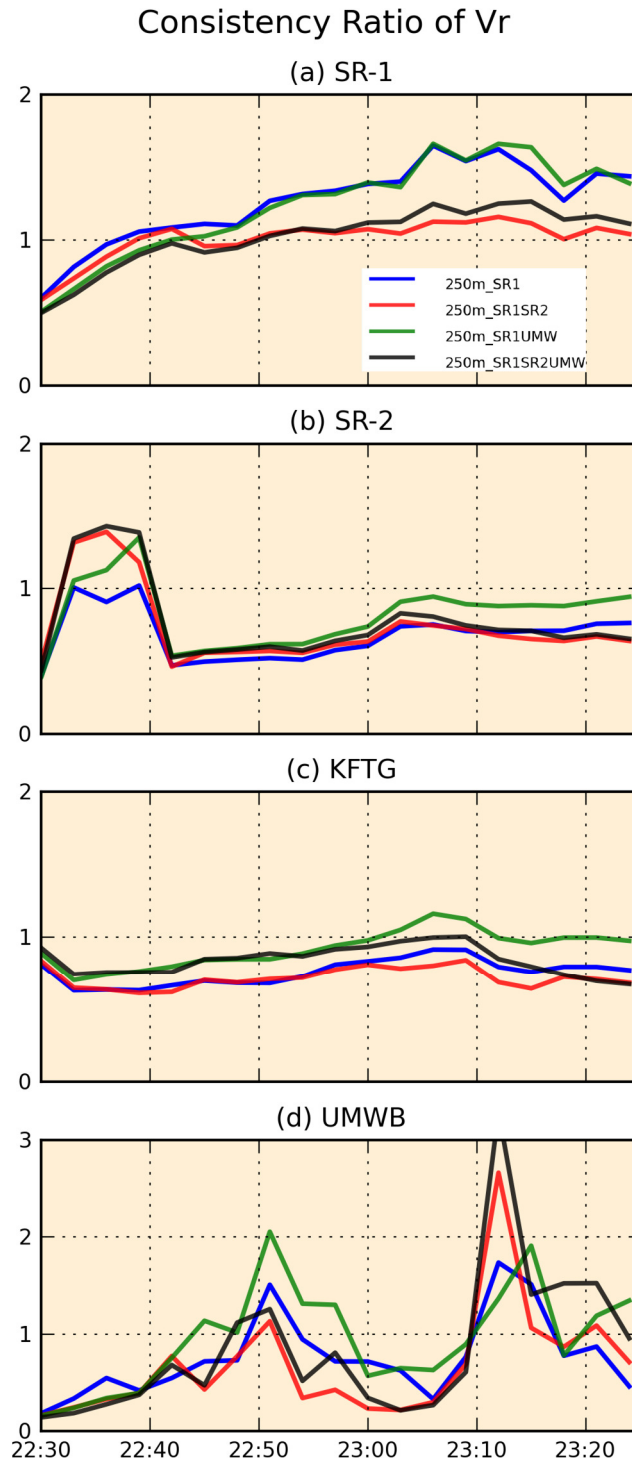


**Fig. 8.** Consistency ratio for  $V_r$  observations from (a) SR1, (b) SR2, (c) KFTG, and (d) UMW for experiments SR1 (blue), SR1SR2 (red), SR1UMW (green), and SR1SR2UMW (black).

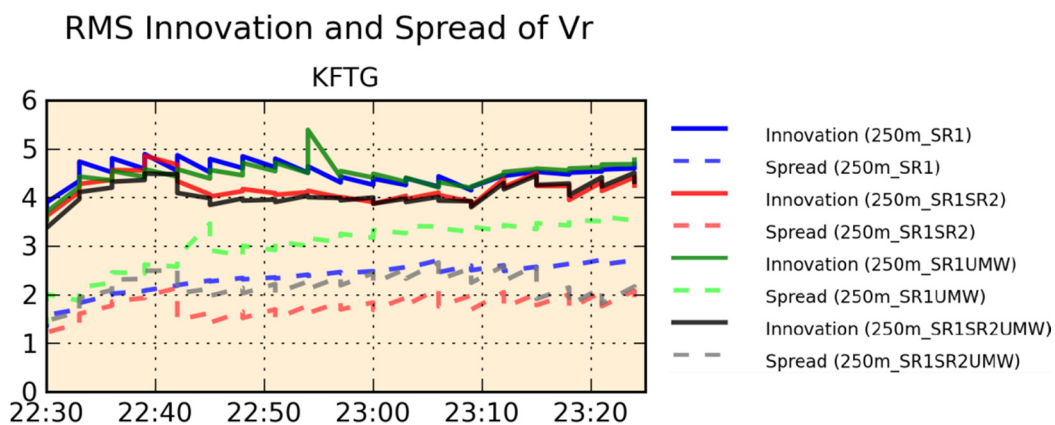


**Fig. 9.** Innovation (solid lines) and spread (dashed lines) calculated against KFTG  $V_r$  (in  $\text{m s}^{-1}$ ) for the four experiments. Coloring is as in Fig. 8.

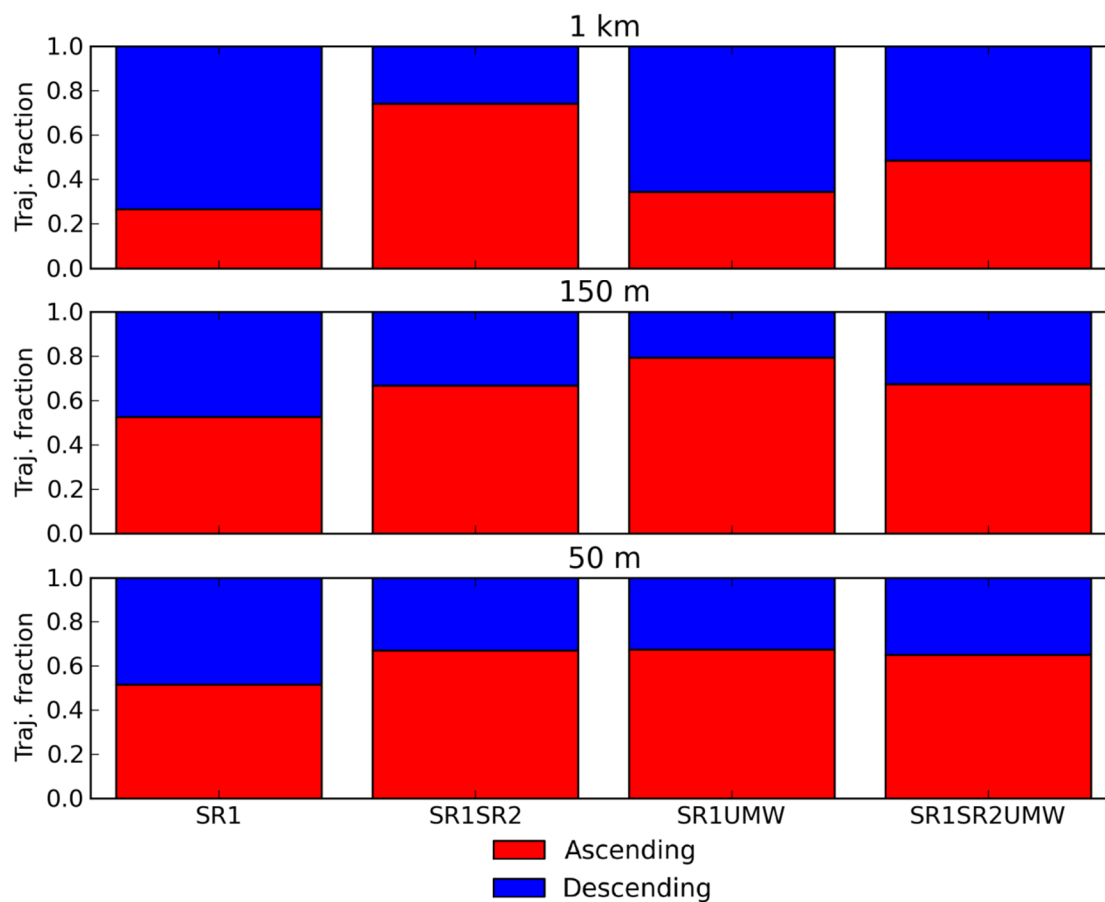


**Fig. 10.** Fraction of backwards trajectories ascending (red) or descending (blue) for each experiment, stratified by initialization height.



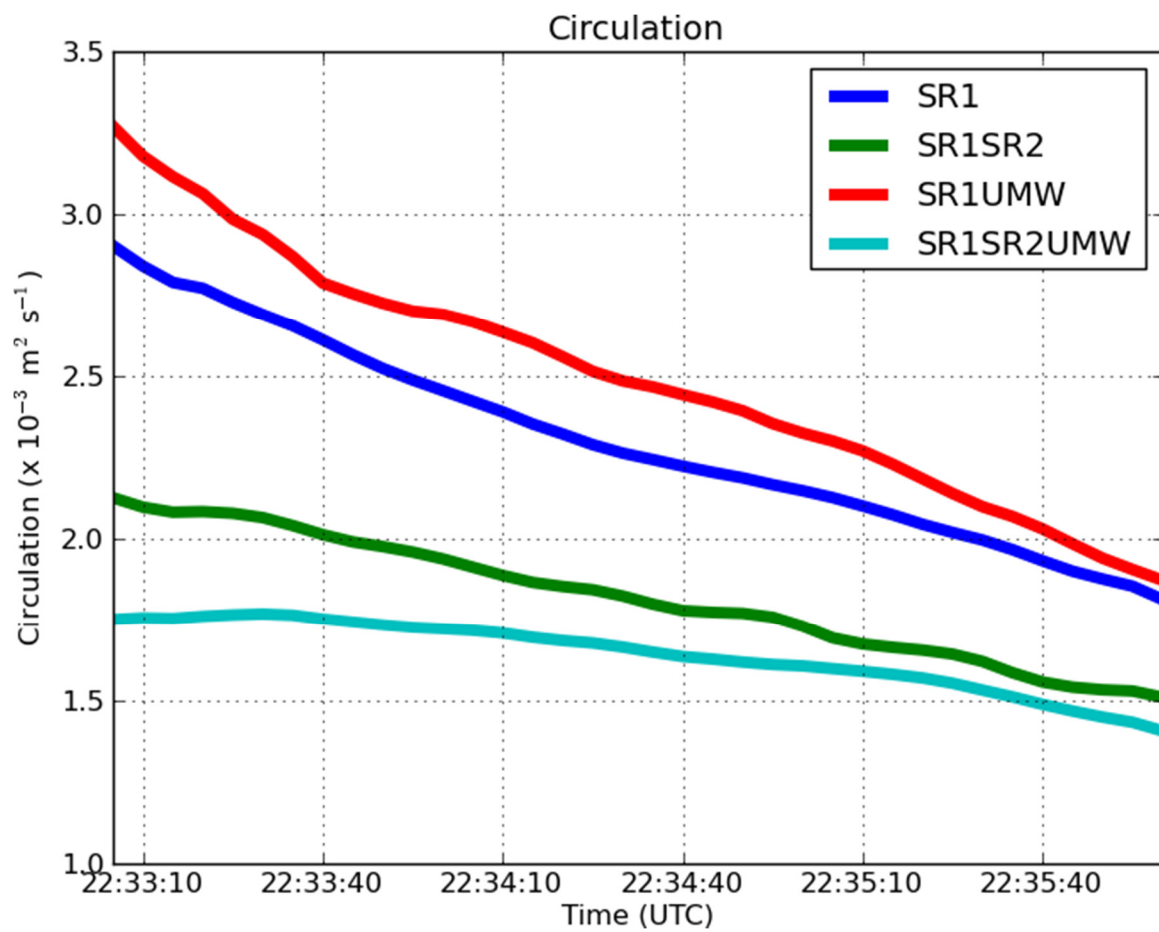


Fig. 11. Ensemble mean circulation about backwards trajectory rings initialized around the vorticity maximum at 150 m AGL.